PROCEEDINGS — OF — **THE ROYAL SOCIETY** A | MATHEMATICAL, PHYSICAL & ENGINEERING SCIENCES

Microstructural level response of HMX−Estane polymer-bonded explosive under effects of transient stress waves

A. Barua, Y. Horie and M. Zhou

References	**This article cites 18 articles** http://rspa.royalsocietypublishing.org/content/468/2147/3725.full.html#ref-list-1
Subject collections	Articles on similar topics can be found in the following collections materials science (115 articles) mechanical engineering (141 articles)
Email alerting service	Receive free email alerts when new articles cite this article - sign up in the box at the top right-hand corner of the article or click **here**

To subscribe to *Proc. R. Soc. A* go to: **http://rspa.royalsocietypublishing.org/subscriptions**

Microstructural level response of HMX–Estane polymer-bonded explosive under effects of transient stress waves

BY A. BARUA[1], Y. HORIE[2] AND M. ZHOU[1,*]

[1] *The George W. Woodruff School of Mechanical Engineering, Georgia Institute of Technology, Atlanta, GA 30332-0405, USA*
[2] *Air Force Research Laboratory, Munitions Directorate, 2306 Perimeter Road, Eglin Air Force Base, Valparaiso, FL 32542, USA*

The effect of transient stress waves on the microstructure of HMX–Estane, a polymer-bonded explosive (PBX), is studied. Calculations carried out concern microstructures with HMX grain sizes on the order of 200 µm and grain volume fractions in the range of 0.50–0.82. The microstructural samples analysed have an aspect ratio of 5 : 1 (15 × 3 mm), allowing the transient wave propagation process resulting from normal impact to be resolved. Boundary loading is effected by the imposition of impact face velocities of 50–200 m s^{-1}. Different levels of grain–binder interface strength are considered. The analysis uses a recently developed cohesive finite element framework that accounts for coupled thermal–mechanical processes involving deformation, heat generation and conduction, failure in the forms of microcracks in both bulk constituents and along grain/matrix interfaces, and frictional heating along crack faces. Results show that the overall wave speed through the microstructures depends on both the grain volume fraction and interface bonding strength between the constituents and that the distance traversed by the stress wave before the initiation of frictional dissipation is independent of the grain volume fraction but increases with impact velocity. Energy dissipated per unit volume owing to fracture is highest near the impact surface and deceases to zero at the stress wavefront. On the other hand, the peak temperature rises are noted to occur approximately 2–3 mm from the impact surface. Scaling laws are developed for the maximum dissipation rate and the highest temperature rise as functions of impact velocity, grain volume fraction and grain–binder interfacial bonding strength.

Keywords: polymer-bonded explosive; HMX; dynamic response; constitutive modelling; hot spots

1. Introduction

Polymer-bonded explosives (PBXs) are a family of composite materials that consist of explosive crystals held together by a polymer binder. They may be subject to impact loading during manufacturing, machining or transport. The loading regimes are diverse—from a few megapascal up to 10 GPa in magnitude

*Author for correspondence (min.zhou@gatech.edu).

and from a microsecond to milliseconds in duration. Under transient loading conditions, the stress state in the material is not homogeneous. The response of these materials to loading associated with compressive stress waves is important because such events can cause severe damage and the formation of hot spots (Armstrong & Elban 1989; Tarver *et al.* 1996; Baer 2002), which affect the safety and chemical stability of the materials.

Owing to material heterogeneity, the structure of the compressive stress wave resulting from impact loading is complex as it traverses the material. The wave propagates faster in the grains but relatively slowly in the binder. This difference in wave speeds causes the stress wavefront to be diffused over a region that is called the compaction region. The gradients of temperature and energies in this region are sharp and need to be resolved at the grain level, because significant energy dissipation occurs in this region. Behind the compaction region, the average stress is approximately constant. At the grain level, the distribution of stress is quite non-uniform. In general, grains experience high stresses and fracture, leading to subsequent frictional interactions across crack surfaces. Frictional dissipation can be the most important source of heating that leads to local temperature rises and to the formation of hot spots (Dienes *et al.* 2006; Barua & Zhou 2011*a*; Barua *et al.* 2012). The spatial distribution, size and temperature of the hot spots are critical measures for assessing the ignition sensitivity of a PBX (Tarver *et al.* 1996; Menikoff 2004).

The hot spots formed during impact loading may lead to reaction initiation if they have sufficient sizes and temperatures (Tarver *et al.* 1996). If the heat generation rate inside a hot spot is higher than the rate of heat loss due to transport mechanisms, the reaction processes are accelerated (Asay 2010, p. 542). Detonation of the explosive can occur if sufficient heat is generated from the reaction in hot spots. Several studies have focused on the effect of transient waves on the heating in granular beds and on the ignition of PBXs. For example, Benson & Conley (1999) and Menikoff (2001) performed mesoscale simulations of compaction waves in granular HMX. The calculations were used to evaluate the changes in porosity as the shock wave propagates. Impact compression of other materials systems has been investigated, including aluminium and iron oxide mixtures (Austin *et al.* 2006), granular sugar (Trott *et al.* 2007) and Ti/SiC powders (Benson *et al.* 1995). Most of the simulations do not show the high temperature rises to be at levels required for ignition, despite experimental evidence pointing to the contrary (Idar *et al.* 2000). One reason for this discrepancy is that these simulations ignore damage in the microstructures and heat generation owing to frictional dissipation at crack surfaces and sliding interfaces.

Panchadhara & Gonthier (2011) studied the compaction of granular explosives under uniaxial compression, using a Lagrangian finite and discrete element technique. Contact and friction across neighbouring grains are considered. The authors report that while plastic dissipation principally affects the average temperature rise in the material, frictional dissipation affects the high-frequency, high-temperature fluctuations that are likely responsible for combustion initiation.

In order to more accurately predict the reaction initiation of PBXs, damage in the grains must be accounted for as it significantly affects the heating process, especially in later stages of deformation (Wu & Huang 2010). Damage can occur
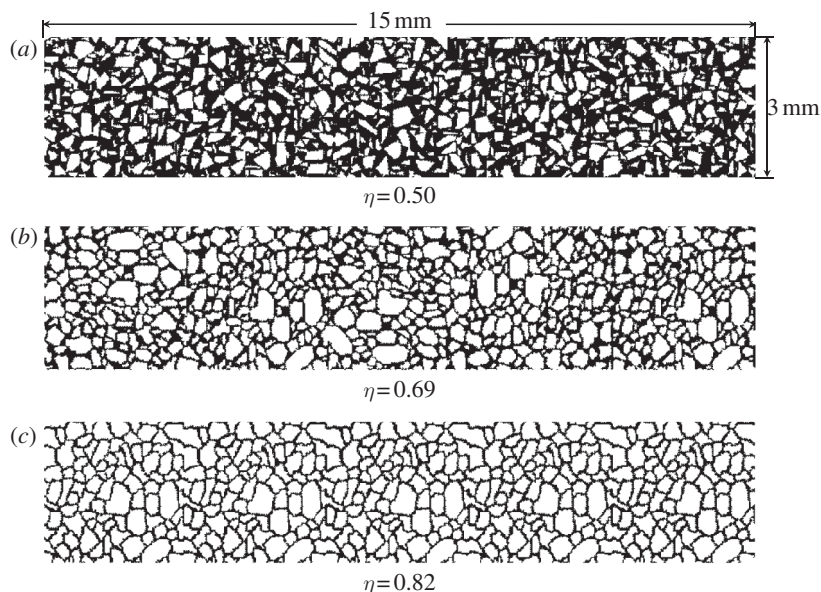
Figure 1. Microstructures having a range of grain volume fractions ($\eta = 0.50$–0.82).

through fracture of grains and debonding along grain–matrix interfaces. Frictional dissipation due to sliding of crack surfaces is an important mechanism for heat generation (Dienes *et al.* 2006). The effect can be more pronounced during transient loading because of the highly non-equilibrium conditions involved. The fracture of grains also leads to the loss of strength of the material, affecting the mechanical integrity of the material. Thus, quantification of the damage at the grain level is important and allows the survivability of explosives under impact loading to be assessed.

Damage at the grain level varies significantly with the loading and microstructure. In particular, the impact velocity, volume fraction of grains in the material, grain size, grain morphology (Khasainov *et al.* 1997; Siviour *et al.* 2004), and the bonding between the binder and the grains are the most important factors. The interplay between these factors is manifested through the field variables, with stress, energy dissipation and temperature being of the primary concern. The dependence of the field variables on the loading and microstructure can be quantified using scaling laws. Such laws can be used in evaluating the performance of explosives under complex loading conditions.

In the analysis reported here, calculations are carried out using microstructures with HMX grain sizes of the order of $200\,\mu\text{m}$ and grain volume fractions in the range of 0.50–0.82. The microstructural samples (figure 1) have an aspect ratio of $5:1$ ($15 \times 3\,\text{mm}$), allowing the transient wave propagation process resulting from normal impact to be resolved. A recently developed Lagrangian cohesive finite element framework is used to quantify the effects of microstructure and thermal–mechanical processes such as matrix deformation, interfacial debonding and fracture of grains on hot spot formation (Barua & Zhou 2011*a*,*b*; Barua *et al.* 2012). Simulations are carried out for a range of load intensity as measured by imposed load face velocity, grain volume fraction and grain/binder interface
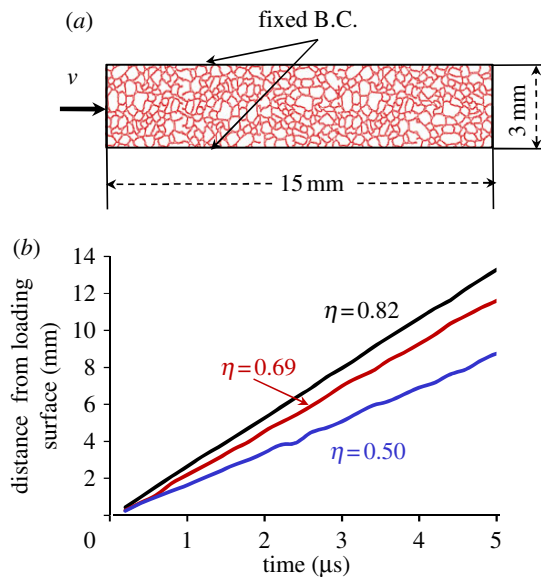
A. Barua et al.

Figure 2. (*a*) Loading configuration and (*b*) the position of stress wavefront as a function of time ($\eta = 0.50$–0.82). (Online version in colour.)

strength. The simulations are used to quantify the stress states, temperature distributions and energy dissipation as the loading wave traverses the length of the microstructure. The focus is on characterizing the spatial and temporal distributions of temperature rises as functions of microstructural and loading attributes. Through the analysis, scaling laws regarding maximum dissipation per unit volume, maximum temperature increase and damage are developed, involving key parameters that quantify loading and microstructure.

2. Configuration of analysis

The calculations are performed on a $15 \times 3\,\text{mm}$ rectangular microstructural region. This sample size is at least one order of magnitude larger than the length scale of the mean grain size for this type of PBX, giving reasonable representation of the microstructures. The loading configuration is shown in figure 2. The specimen is initially stress-free and at rest. Impact loading is effected by applying a constant normal velocity on the left end of the sample. The upper and lower boundaries are constrained such that lateral expansion (up for the upper edge and down for the lower edge) does not occur. This configuration approximates the normal impact loading of an infinitely wide material block under conditions of macroscopic uniaxial strain. The imposed constant boundary/piston velocity approximately simulates loading under a constant input stress level, which will be discussed later. The specimen length is chosen to allow approximately the first 5.5–$8.5\,\mu\text{s}$ of the propagation of the stress wave from the left surface towards the right to be analysed, before the wave arrives at the right end. The calculations capture the effects of transient wave as it propagates through the specimen. This

is a two-dimensional model and the conditions of plane–strain prevail at length scales higher than the size scale of the material heterogeneities.

The calculations use a recently developed cohesive finite element method modelling framework to capture the coupled thermal and mechanical processes in the microstructure (Barua & Zhou 2011*a*; Barua *et al.* 2012). Individual constituents are modelled using Lagrangian elements and fracture and subsequent contacts are tracked explicitly using a contact algorithm. This allows the assessment of the local as well as macro-level response of the composite. Like deformation and heating, arbitrary crack patterns or crack paths can be predicted and tracked as they occur as an outcome of applied loading. The forms of fracture tracked include (i) failure of each grain through multiple crack paths; (ii) debonding along grain–binder interfaces; and (iii) cracking of the binder (cracks within the binder interior). This is achieved through cohesive elements embedded between regular bulk finite elements inside the grains, between the grains and the binder, and inside the binder. Each type (grain–grain, grain–binder, binder–binder) of cohesive elements has its own interfacial track–separation relation (constitutive law of the interface). This relation specifies (i) the energy required to create a unit area of crack surface (fracture energy); (ii) maximum strength of the interface; and (iii) critical separation (shear, normal or combined) needed to cause complete fracture. This relation serves as the 'fracture criterion' such that no other fracture criterion needs to be specified as part of the model. Because the cohesive elements are distributed throughout the whole model, arbitrary crack/microcrack patterns can be tracked.

The bilinear traction–separation law developed by Zhai *et al.* (2004) is used in the case of tensile and shear separations. Under compression, a penalty traction is used to strongly discourage the interpenetration of cohesive surfaces. Failure of cohesive elements results in creation of new surfaces. In order to prevent the interpenetration of failed surfaces, a contact algorithm is used to apply a normal penalty force to prevent the overlap of elements. The Coulomb friction law is used to determine the frictional force between contacting surface pairs.

The binder is modelled using a finite deformation viscoelastic model. A Prony series model developed by Mas & Clements (1996) is used to characterize the variation of the shear modulus with the relaxation time. For the HMX granules, a hyperelastic constitutive model is used. This study focuses on non-shock conditions; therefore, the HMX grains undergo very little plastic deformation, justifying the use of a hyperelastic model for the HMX grains. However, the grains are allowed to fracture according to the prescribed cohesive traction–separation law. The constitutive parameters for HMX, Estane and the cohesive interface properties are given in Barua & Zhou (2011*a*).

3. Microstructures analysed

Three different microstructures with grain volume fractions $\eta = 0.50$, 0.69 and 0.82, respectively, are used. The micrographs corresponding to $\eta = 0.69$ and 0.82 are obtained from digitized microstructures of actual PBX specimens and are similar to those used in (Barua & Zhou 2011*a*). The micrograph with $\eta = 0.50$ is created using two-dimensional Voronoi tessellation. This approach allows multifaceted grains with morphologies similar to those of actual HMX grains to
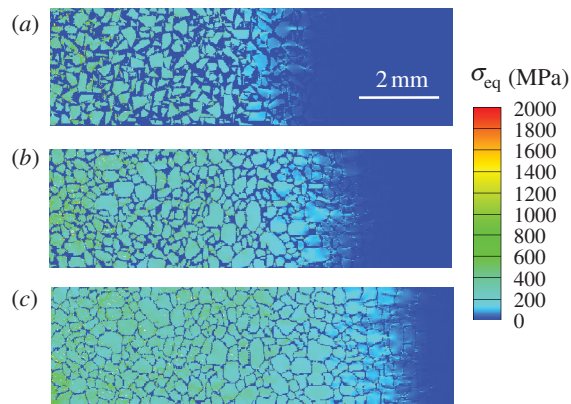
A. Barua et al.

Figure 3. Distribution of equivalent stress at $t = 3.6\,\mu s$ for varying packing densities, η (*a*) 0.50, (*b*) 0.69 and (*c*) 0.82 ($v_0 = 200\,\mathrm{m\,s^{-1}}$). (Online version in colour.)

be obtained. The desired volume fraction is attained by increasing or decreasing the size of the grains. Previously, Wu & Huang (2009) used a similar approach to generate idealized PBX microstructures. The grain sizes for the earlier-mentioned microstructures have a mean value of approximately $200\,\mu m$ and are used together to analyse the effect of grain volume fraction on the transient response of PBXs.

4. Results and discussion

A parametric study is carried out, focusing on the effects of (i) strain rate; (ii) grain volume fraction ($\eta = 0.50$–0.82); and (iii) interface strength. For all calculations presented, the initial temperature is $T_i = 300\,\mathrm{K}$. The velocity v_0 of the left surface is varied between 50 and $200\,\mathrm{m\,s^{-1}}$, yielding overall strain rates of $\dot{\varepsilon} = (3.33 - 13.3) \times 10^3\,\mathrm{s^{-1}}$. The velocity is imposed at the left surface of the configurations in figure 2, with a linear ramp from zero to v_0 in the first $2\,\mu s$ of loading. The strength of the grain/matrix interface is varied by altering the maximum allowed surface traction S_{max} at the interface from 8.75 to $35.0\,\mathrm{MPa}$ (refer to table 2 of Barua & Zhou (2011*a*)). This range of values represents weakly to strongly bonded interfaces. Unless otherwise stated, the value of S_{max} is taken as $35.0\,\mathrm{MPa}$.

Because this analysis focuses on the transient response of PBX microstructures, the discussions are limited to times before the stress wave reaches the boundary on the right (figure 2*a*). The overall velocity of the stress waves in the microstructure varies with the grain volume fraction and the interface bonding strength between the phases. Figure 2*b* shows the location of the stress wave as a function of time, for $\eta = 0.50$–0.82, and $S_{max} = 35.0\,\mathrm{MPa}$. The slopes of the curves correspond to the wave speeds in the respective microstructures. Clearly, the wave speed increases with grain volume fraction. For instance, if the grain volume fraction is $\eta = 0.82$, the wave velocity is $2.65 \times 10^3\,\mathrm{m\,s^{-1}}$. In comparison, the elastic longitudinal wave speed in HMX is approximately $3.5 \times 10^3\,\mathrm{m\,s^{-1}}$. The time taken by the wave to reach the right surface is $5.6\,\mu s$. The results presented here correspond to times up to $3.6\,\mu s$, ensuring that the focus is on the transient response of the specimen.
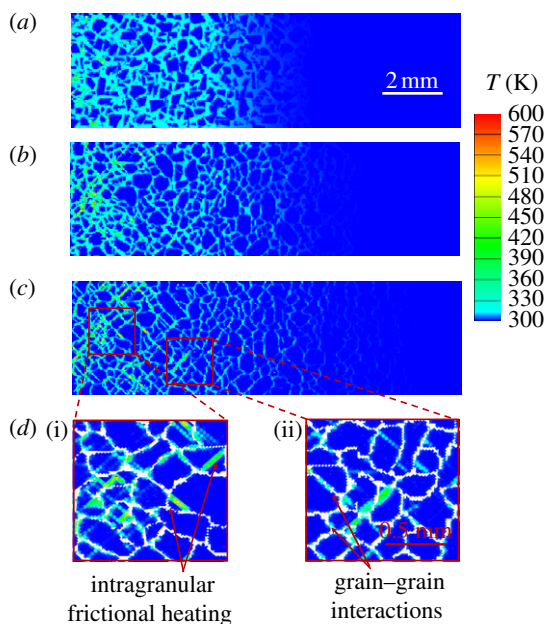
Figure 4. Distribution of temperature at $t = 3.6\,\mu s$ for varying packing densities, η: (*a*) 0.50, (*b*) 0.69 and (*c*) 0.82 and (*d*) close-up view of the grains in two regions showing (i) transgranular fracture and frictional heating along crack faces and (ii) localized heating due to grain–grain interactions ($v_0 = 200\,\mathrm{m\,s^{-1}}$). (Online version in colour.)

A set of calculations using different grain volume fractions is presented to delineate the processes at hand. Figures 3 and 4 illustrate the distributions of stress and temperatures in the microstructure for packing densities of $\eta = 0.50$, 0.69 and 0.82 at $t = 3.6\,\mu s$ for an impact velocity $v_0 = 200\,\mathrm{m\,s^{-1}}$. Clearly, for the higher grain volume fractions, the stress waves have propagated over a longer distance in the same amount of time. At the stress wavefront, the intensity is low initially and gradually increases to a peak value. Force chains are formed in the compaction region. Behind the compaction region, the stress in each phase is higher and has no long-term structure, with the harder grains carrying higher levels of stress. As the grain volume fraction increases, the overall stress level in the grains also increases. The higher stresses result in a higher tendency for transgranular fracture and frictional dissipation.

In contrast to the stress profiles, the temperature rises are highest near the impact surface and gradually decrease away from it. When the grain volume fraction is low (e.g. $\eta = 0.50$), the stresses in the grains are not high enough to cause fracture and most of the temperature rise is due to viscoelastic dissipation in the binder. Because the amount of viscoelastic dissipation is time-dependent, the highest temperature rises occur near the impact surface. This observation is only for the time durations for which the stress wave is still propagating towards unstressed materials and no wave reflection occurs. This is to say that the sample size is relatively large for the time duration of interest. Such scenarios are quite relevant because when the impact velocity is high, ignition can occur within a short time upon contact, and the stress wavefront may not have reached

any boundary of the sample yet. We note that that in Barua & Zhou (2011*a*) and Barua *et al.* (2012), the conditions are such that stress waves reflect from opposite boundaries of the samples for the time duration analysed. Under those conditions, the highest temperature may not be at the impact face. Additionally, higher packing densities ($\eta = 0.69$, 0.82) lead to higher overall stresses and transgranular fracture and frictional dissipation at the fractured surfaces, even at the same impact velocity. This causes severe temperature rises of the order of 300–400 K to occur in the grains. Two regions of the microstructure with $\eta = 0.82$ are shown in figure 4*d* at a higher magnification to highlight the failure mechanisms (transgranular fracture and sliding frictional heating along crack faces, intergranular interaction and heating due to binder deformation and crack face friction) captured.

The distributions of stress and temperature in the specimen vary significantly with time and distance from the impact surface. One way to represent the variation of stress in the specimen is to analyse the average stress across the width of the specimen along the loading (horizontal) direction. For this purpose, the average value across the width (perpendicular to the direction of loading) of the specimen for each field variable (e.g. equivalent stress) is computed. Figure 5*a* shows the stress profiles at different times between $t = 1.2$–6.0 µs, for $\eta = 0.82$ and $v_0 = 100 \, \text{m s}^{-1}$. The stress profiles are qualitatively similar as the wave propagates. In the compaction region, the stress increases gradually from zero to a peak value over a distance of approximately 5 mm. Behind this region, the average stress is approximately constant, at around 200 MPa. The length of the compaction region is important because it determines the gradient across which the stress and temperature rises occur. A sharper gradient usually corresponds to higher amounts of fracture and damage. The length of the compaction region does not vary significantly with time, because (i) the microstructure is approximately homogeneous at the length scale of several grains and (ii) the time scales considered here are not sufficient for any significant attenuation of the stress wave. Finally, as the wave reaches the fixed surface on the right, it is reflected back, and the stress state in the specimen tends to a nominally homogeneous one.

Figure 5*b* shows the average stress profiles at $t = 3.6$ µs for three calculations with boundary velocities—$v_0 = 50$–200 m s^{-1} and $\eta = 0.82$. At a higher boundary velocity, the viscoelastic binder is harder, leading to higher stresses. The average stress behind the compaction region increases from 120 to 280 MPa as the impact velocity is increased from 50 to 200 m s^{-1}. The length of the compaction region is similar for all boundary velocities. Thus, higher impact velocities correspond to a much sharper increase of stress across the compaction region, leading to more damage and frictional dissipation.

Figure 5*c* plots the average stress profiles at $t = 3.6$ µs for different volume fractions between $\eta = 0.5$–0.82 and $v_0 = 100 \, \text{m s}^{-1}$. The average stress increases with grain volume fraction. The length of the compaction zone does not change significantly with grain volume fraction. The average stress increases from 100 to 200 MPa as the grain volume fraction increases from 0.5 to 0.82. For higher grain volume fractions, the higher wave speeds result in dissipation and temperature rises occurring over a larger area in the same amount of time.

The stress profiles at $t = 3.6$ µs for interface strengths from $S_{\text{max}} = 8.75$– 35.0 MPa, $\eta = 0.82$ and $v_0 = 200 \, \text{m s}^{-1}$ are shown in figure 5*d*. At higher interface strength values, the material is able to sustain higher stresses without fracture.
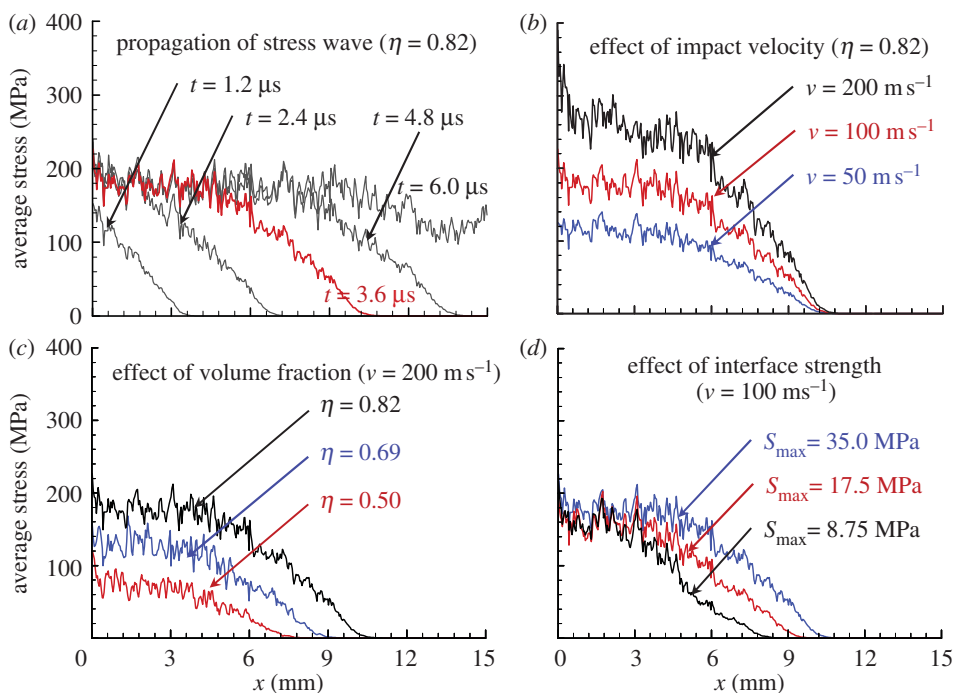
Figure 5. Variation of equivalent stress with distance from the impact surface for (*a*) different times: $t = 1.2$–$6.0\,\mu s$ ($\eta = 0.82$, $v = 100\,\mathrm{m\,s^{-1}}$); (*b*) different impact velocities: $v_0 = 50$–$200\,\mathrm{m\,s^{-1}}$ ($\eta = 0.82$, $t = 3.6\,\mu s$); (*c*) different packing densities: 0.50–0.82 ($v_0 = 200\,\mathrm{m\,s^{-1}}$, $t = 3.6\,\mu s$); and (*d*) different interface strengths: $S_{\mathrm{max}} = 8.75$–$35.0\,\mathrm{MPa}$ ($\eta = 0.82$, $v_0 = 100\,\mathrm{m\,s^{-1}}$, $t = 3.6\,\mu s$). (Online version in colour.)

Consequently, the wave speed increases by a factor of 1.3 (from 50 to $200\,\mathrm{m\,s^{-1}}$) over the interface strength range analysed. The compaction region is more spread out in cases with higher interface strengths. Behind the compaction region, the stress levels are essentially the same for the values of interface strength considered. This is due to the crack closure effect of the compressive loading. For instance, for a low interface bonding strength, a greater amount of debonding occurs. However, crack surfaces are in compression, resulting in the stress carried by the material being similar to that carried by an undamaged material. Consequently, the average stress in the material is primarily dependent on the volume fraction and the impact velocity, and is not significantly affected by the strength of the bonding between the different constituents.

Figure 6 shows the effect of the boundary velocity ($v_0 = 50$–$200\,\mathrm{m\,s^{-1}}$) on the average stress in the grains for $\eta = 0.5$, 0.69 and 0.82. A scaling law equation (4.1) is developed to quantify the average stress as a function of the grain volume fraction, η and boundary velocity, v_0:

$$\sigma_{\mathrm{avg}} = \sigma_{\mathrm{avg}}^0 \left(\frac{\eta}{\eta_{\mathrm{ref}}} + 1 \right)^{2.5} \left(\frac{v_0}{v_{\mathrm{ref}}} \right)^{0.8}. \tag{4.1}$$
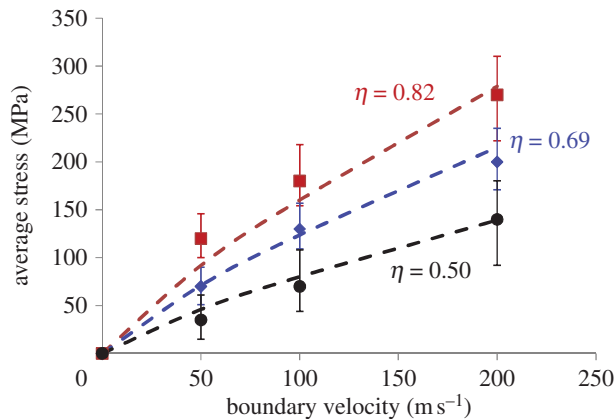
　　　　　　　　　　　　A. Barua et al.

Figure 6. Variation of average stress with boundary velocity grain and volume fraction. (Online version in colour.)

Table 1. Parameters in equations (4.1)–(4.3).

parameter	value	unit
η_{ref}	0.5	—
v_{ref}	90	$m\,s^{-1}$
S_{max}^{ref}	35	MPa
t_d	1.6	s
σ_{avg}^0	13	MPa
T_0	1.55	K
W_f^0	0.025	$MJ\,m^{-3}$

This relationship consists of dimensionless terms obtained by normalizing η and v_0 by reference values η_{ref} and v_{ref}, respectively. The parameters in equation (4.1) are listed in table 1. Over the range of conditions analysed, the interface bonding strength does not affect the average stress; therefore, it is not included in equation (4.1). Overall, the average stress increases with volume fraction η and boundary velocity v_0. The average stress has a slight nonlinear dependence on v_0 as shown by the exponent of 0.8 in equation (4.1) (figure 6). This nonlinearity is primarily due to the rate-dependence of the viscoelastic binder.

On the other hand, the average stress is quite sensitive to the volume fraction of the grains, as indicated by the exponent of 2.5. The high sensitivity can be explained based on the difference in the mechanisms responsible for transmission of stress at low- and high-grain volume fractions. When η is low (less than or equal to 0.5), the softer matrix is primarily responsible for carrying and transmitting stress. While at high values of η (0.69, 0.82), stress is preferentially transmitted across neighbouring grains by means of forming force chains. Consequently, there is a large variation in the average stress with a small increase in grain volume fraction. For instance, the average stress increases approximately by a factor of 2 as the grain volume fraction is increased from 0.5 to 0.69.
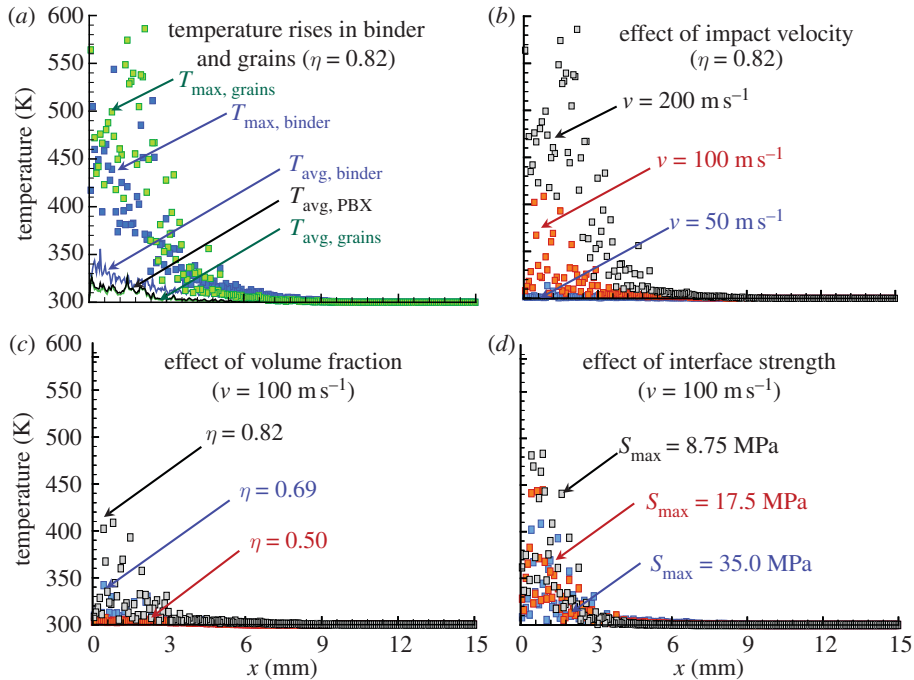
Figure 7. Peak temperature in the microstructure at different distances from the impact surface (*a*) in grains and binder at $t = 3.6 \, \mu s$ ($\eta = 0.82$, $v_0 = 200 \, \mathrm{m \, s^{-1}}$); (*b*) for different impact velocities: $v_0 = 50$–$200 \, \mathrm{m \, s^{-1}}$ ($\eta = 0.82$, $t = 3.6 \, \mu s$); (*c*) for different packing densities: 0.50–0.82 ($v_0 = 100 \, \mathrm{m \, s^{-1}}$, $t = 3.6 \, \mu s$); and (*d*) for different interface strengths: $S_{max} = 8.75$–$35.0 \, \mathrm{MPa}$ ($\eta = 0.82$, $v_0 = 100 \, \mathrm{m \, s^{-1}}$, $t = 3.6 \, \mu s$). (Online version in colour.)

The heterogeneity in the microstructure at the grain level gives rise to highly localized temperature distributions. Chemical reactions initiate in localized hot spots, characterized by high rises in temperature. The temperature rises need to be analysed at both the grain level and the macro level, using different metrics. Possible measures include (i) temperature rise (ΔT) as a function of distance from the loading surface and (ii) the overall temperature rise in the microstructure measured by mass fraction having a certain temperature rise. The peak temperature rise can be used to identify locations that are most susceptible to ignition. The overall temperature rise can be used to identify the contribution of the different heating mechanisms. Two heating mechanisms are considered here: viscoelastic dissipation in the binder, and frictional dissipation along contact surfaces. The viscoelastic dissipation results in bulk temperature rise in the binder, which can be conducted into the grains through the grain–matrix interfaces. On the other hand, frictional dissipation occurs locally along crack faces and is responsible for much of the heating in the composite, especially at higher strains.

Figure 7*a* shows the average and maximum temperature rises at $t = 3.6 \, \mu s$ in the constituents for a microstructure with $\eta = 0.82$ at a boundary velocity of $v_0 = 200 \, \mathrm{m \, s^{-1}}$. The average temperature is typically low, at approximately 350 K. However, the maximum temperature in the grains

can be very high, up to 600 K. This is higher than the maximum temperature in the matrix, which is approximately 550 K. The viscoelastic dissipation associated with the matrix is typically less intense compared with frictional dissipation occurring as a result of transgranular fracture of the grains. In general, the average temperature in the grains and matrix is highest near the impact surface and decreases gradually with distance away from it. However, the highest temperature rises are at approximately 2–3 mm from the impact surface. The peak temperatures are highly stochastic, but overall, are highest near the impact surface and gradually decrease away from it. The position of the wavefront at 3.6 µs is at a distance of 10.5 mm from the impact surface (figure 5b). However, at this time, the temperature rise is not significant for distances greater than 5 mm from the impact surface. Because processes associated with friction and heat conduction occur at much slower time scales compared with stress wave propagation, frictional heating and heat conduction determine the time scale of delayed combustion of PBXs during non-shock loading (Idar *et al.* 2000).

Figure 7b shows the effect of the boundary velocity ($v_0 = 50$–$200\,\mathrm{m\,s}^{-1}$) on the maximum temperature rises in the grains at $t = 3.6\,\mu\mathrm{s}$ for $\eta = 0.82$. At the low-impact velocity of $50\,\mathrm{m\,s}^{-1}$, the maximum temperature recorded is approximately 310 K, while at 100 and $200\,\mathrm{m\,s}^{-1}$, the corresponding temperatures are approximately 400 and 600 K, respectively. The large differences in peak temperature at low- and high-impact velocities suggest that the transition of heating mechanism from viscoelastic to frictional dissipation occurs much earlier at high-impact velocities. This will be quantified later in the section.

Figure 7c shows the peak temperatures in HMX for varying volume fractions, $\eta = 0.50$–0.82, at a boundary velocity of $100\,\mathrm{m\,s}^{-1}$. Clearly, higher volume fractions correspond to higher temperature rises. For $\eta = 0.82$, peak temperatures near the impact surface can reach 400 K, whereas for $\eta = 0.50$, the corresponding peak temperatures are less than 310 K. Once fracture and frictional dissipation initiates, severe temperature rises occur in the grains. The temperature rise occurring in the microstructure increases with grain volume fraction; however, the variation itself is highly nonlinear, with a lower rate of temperature rise during viscoelastic dissipation, followed by a higher rate of heating during frictional dissipation.

Figure 7d shows the maximum temperatures at $t = 3.6\,\mu\mathrm{s}$ for samples with different interface strengths in the range of $T_{\max} = 8.75$–$35.0\,\mathrm{MPa}$ and $\eta = 0.82$. The impact velocity is $v_0 = 100\,\mathrm{m\,s}^{-1}$. The material with lower interface strength suffers more damage, leading to a greater amount of frictional dissipation and higher temperature rises. The maximum temperature generally increases as the interface strength decreases. For this set of calculations, the maximum temperature increases from 400 to 500 K as the interface strength is decreased by a factor of 4, from 35.0 to 8.75 MPa.

The critical (ignition) temperature for HMX under a constant heat flux is estimated to be approximately 775 K (Dienes *et al.* 2006). The heat generation rate due to frictional dissipation in the current setting varies with time. Nevertheless, the results strongly suggest that frictional heating can lead to temperature rises in the grains that are sufficient for melting and reaction initiation. The preceding results can be used to obtain a quantification of the maximum hot-spot temperature as a function of loading and microstructure.

Specifically, the evolution of peak temperature rise can be expressed as a function of grain volume fraction, boundary velocity, interface bonding strength:

$$T_{\text{max, grains}} = \begin{cases} 0, & t < t_{\text{d}} \\ T_{\text{i}} + T_0 \left(\dfrac{\eta}{\eta_{\text{ref}}} + 1 \right)^{5.0} \left(\dfrac{v_0}{v_{\text{ref}}} \right)^{1.3} \left(\dfrac{S_{\text{max}}}{S_{\text{max}}^{\text{ref}}} + 1 \right)^{-1} \left(\dfrac{t}{t_{\text{d}}} - 1 \right)^2, & t \geq t_{\text{d}}. \end{cases}$$

(4.2)

Here, dimensionless terms are obtained by normalizing η, v_0, S_{max} and t, using reference values η_{ref}, v_{ref}, $S_{\text{max}}^{\text{ref}}$ and delay time t_{d}. T_{i} is the initial temperature 300 K. The parameters in equation (4.2) are also listed in table 1. Equation (4.2) highlights the effect of the delay time. Temperature rise is negligible until a t_{d} has elapsed. Beyond t_{d}, the temperature rise is proportional to the second power of time. The peak temperature rise is highly sensitive to the grain volume fraction η. This can be attributed to the high sensitivity of the average stress to η (as seen in equation (4.1)), which results in a higher amount of frictional dissipation at the fractured surfaces. The variation of peak temperature with impact velocity is almost linear. The maximum temperature bears an inverse relationship with the interface bonding strength. A decrease in interface bonding strength leads to a higher amount of fracture at the grain–matrix interface. The resulting frictional dissipation causes higher temperature rises at the fractured surfaces.

The preceding discussions make it clear that a significant amount of energy is dissipated as a result of fracture and friction at interfaces. To quantify the evolution of damage, the distribution of fracture energy is plotted along the length of the specimen. Figure 8a shows the result for a microstructure with $\eta = 0.69$ at $v_0 = 200 \, \text{m s}^{-1}$. The fracture energy is highest near the impact surface and gradually decreases to zero at the front of the stress wave. At $t = 3.6 \, \mu\text{s}$, the fracture energy is approximately $4 \, \text{MJ m}^{-3}$ near the impact surface and approximately $0.5 \, \text{MJ m}^{-3}$ at 4 mm from the impact surface. The fracture energy at each location increases with time. As the impact velocity increases from 50 to $200 \, \text{m s}^{-1}$, the amount of energy dissipated through fracture increases (figure 8b). For example, at a distance of 2 mm from the loading surface, the fracture energy is approximately 3.0 and $0.5 \, \text{MJ m}^3$ for impact velocities of 100 and $200 \, \text{m s}^{-1}$, respectively.

Figure 8c shows the fracture energy at $t = 3.6 \, \mu\text{s}$ for microstructures with grain volume fractions $\eta = 0.50$–0.82 for $v_0 = 200 \, \text{m s}^{-1}$. For both $\eta = 0.69$ and 0.82, the fracture energy is approximately $4 \, \text{MJ m}^{-3}$ near the impact surface. However, along the length of the specimen, fracture energy is lower for lower grain volume fractions.

Figure 8d shows the fracture energy dissipated at $t = 3.6 \, \mu\text{s}$ for samples with different interface bonding strengths ($T_{\text{max}} = 8.75$–35.0 MPa) and $\eta = 0.82$ at $v_0 = 200 \, \text{m s}^{-1}$. When $T_{\text{max}} = 8.75$ MPa, a higher amount of fractured surfaces are generated when compared with the case in which with $T_{\text{max}} = 35.0$ MPa. However, the amount of energy dissipated per unit area of crack extension is lower when the interface strength is lower. This causes the distribution of fracture energy to remain approximately invariant over the range of interface strengths considered, as seen in the figure.

The fracture energy varies non-uniformly with time and distance along the loading direction. As mentioned earlier, it is highest at the impact surface and
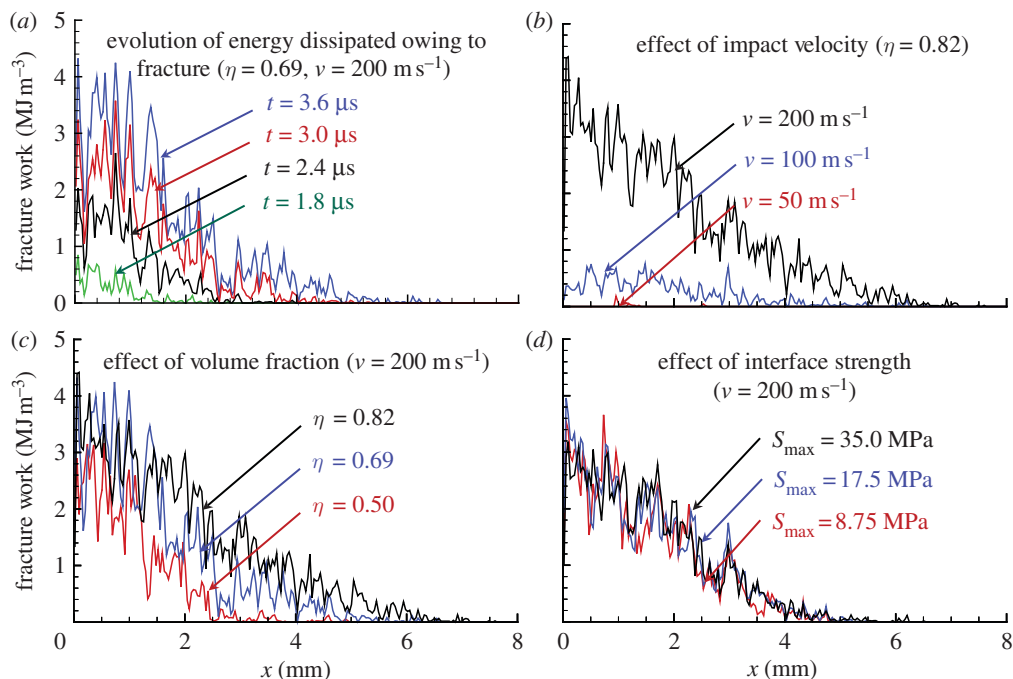
Figure 8. Variation of fracture energy along the loading direction for (*a*) different times: $t = 1.8$–$3.6\,\mu s$ ($\eta = 0.69$, $v_0 = 200\,m\,s^{-1}$); (*b*) different impact velocities: $v_0 = 50$–$200\,m\,s^{-1}$ ($\eta = 0.82$); (*c*) different packing densities: 0.50–0.82 ($v_0 = 200\,m\,s^{-1}$, $t = 3.6\,\mu s$); and (*d*) different interface strengths: $S_{max} = 8.75$–$35.0\,MPa$ ($\eta = 0.82$, $v_0 = 200\,m\,s^{-1}$, $t = 3.6\,\mu s$). (Online version in colour.)

gradually decreases to zero at the front of the stress wave. The variation of fracture energy dissipated at the impact surface can be quantified using the dimensionless terms used in equations (4.1) and (4.2) as follows:

$$W_{\mathrm{f}} = \begin{cases} 0, & t < t_{\mathrm{d}} \\ W_{\mathrm{f}}^0 \left(\dfrac{\eta}{\eta_{\mathrm{ref}}} + 1 \right)^{1.9} \left(\dfrac{v_0}{v_{\mathrm{ref}}} \right)^4 \left(\dfrac{t}{t_{\mathrm{d}}} - 1 \right)^{1.2}, & t \geq t_{\mathrm{d}}. \end{cases} \tag{4.3}$$

The effect of delay time is similar in both equations (4.2) and (4.3); the fracture energy does not initiate before a t_{d} has elapsed. In contrast to the evolution of average stress and peak temperature, the fracture energy has a high sensitivity to the impact velocity, as shown by the exponent of 4. At the same time, a higher impact velocities results in a higher nominal strain; this in turn causes an increased fracture of grains and debonding along the interfaces. The fracture energy also increases nonlinearly with volume fraction, as shown by the exponent of 1.9. The increase of fracture energy is almost linear with time. The interface bonding strength does not significantly affect the fracture energy and is not included in equation (4.3). It is noted that, for most of the calculations, the corresponding fits are obtained up to a time of 5–6 μs. Additional failure mechanisms may become active at higher strains, affecting hot spot formation beyond the range analysed here.
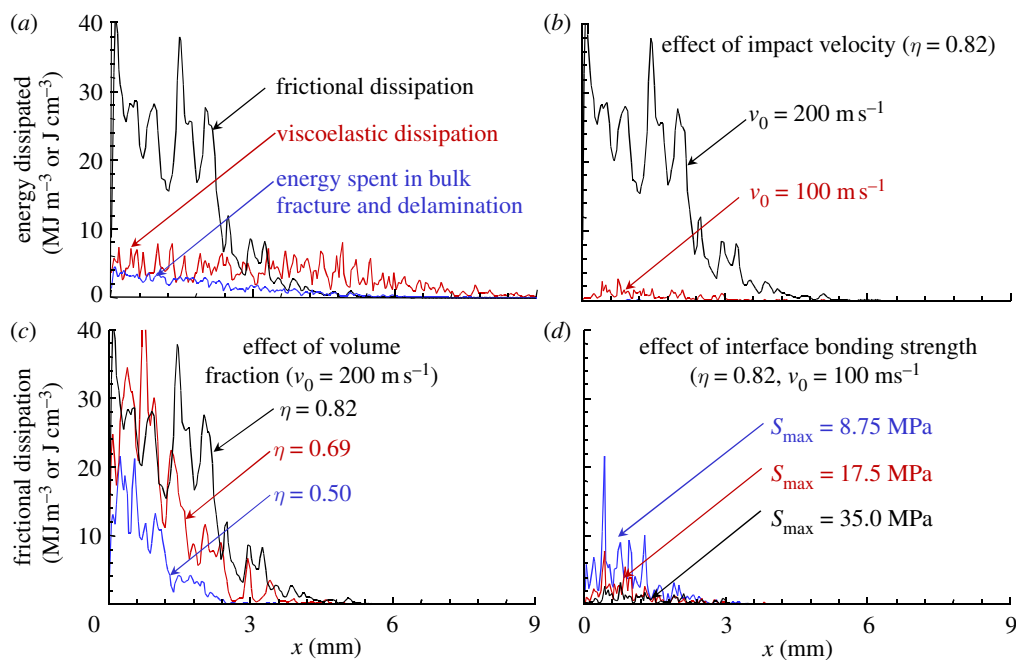
Figure 9. Variation of energy dissipated at different distances from the impact surface for (a) all forms of dissipation at $t = 3.6\,\mu s$ ($\eta = 0.82$, $v_0 = 200\,\mathrm{m\,s^{-1}}$), ($b$) different impact velocities: $v_0 = 50$–$200\,\mathrm{m\,s^{-1}}$ ($\eta = 0.82$); (c) different packing densities: 0.50 and 0.82 ($v_0 = 200\,\mathrm{m\,s^{-1}}$, $t = 3.6\,\mu s$); and (d) different interface strengths between $S_{max} = 8.75$–$35.0\,\mathrm{MPa}$ ($\eta = 0.82$, $v_0 = 100\,\mathrm{m\,s^{-1}}$, $t = 3.6\,\mu s$). (Online version in colour.)

The evolution of temperature is directly related to the dissipation of energy. Figure 9a shows the different forms of energy dissipated at $t = 3.6\,\mu s$, including cohesive energy spent on causing fracture, frictional and viscoelastic dissipations—for a microstructure with $\eta = 0.82$ subject to a boundary velocity of $v_0 = 200\,\mathrm{m\,s^{-1}}$. Frictional dissipation is the dominant mechanism of heat generation, followed by viscoelastic dissipation. The amount of fracture energy dissipated is also highest near the impact surface and decreases approximately linearly with distance away from the surface. The viscoelastic dissipation per unit volume of approximately $6\,\mathrm{MJ\,m^{-3}}$ is highest near the impact surface and gradually decreases with distance away from the impact surface. Because viscoelastic dissipation is a form of bulk dissipation, it results in a more uniform distribution of temperature in the binder, in contrast to the distribution of frictional dissipation that occurs along interfaces.

Because frictional dissipation is responsible for high-temperature rises, we focus on its variation with the impact velocity and loading conditions. Figure 9b shows the variation of frictional dissipation along the length of the specimen at $t = 3.6\,\mu s$ for different impact velocities in the range of $v_0 = 50$–$200\,\mathrm{m\,s^{-1}}$ and $\eta = 0.82$. At $v_0 = 100\,\mathrm{m\,s^{-1}}$, the delay time for the onset of frictional heating is long (figure 10) and no significant frictional dissipation occurs. At higher impact velocities, frictional dissipation is significant. For instance, as the impact velocity is increased from 100 to $200\,\mathrm{m\,s^{-1}}$, frictional dissipation near the impact surface
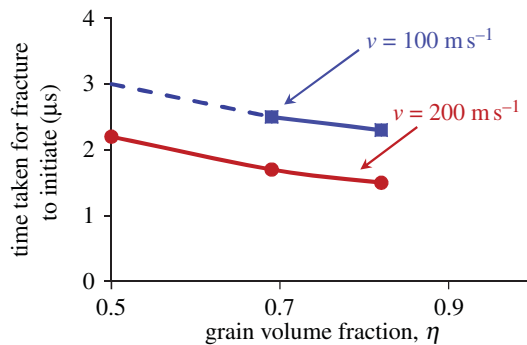
A. Barua et al.

Figure 10. Variation of delay time (t_d) with grain volume fraction and boundary velocity. (Online version in colour.)

increases by almost an order of magnitude, from less than $3\,\mathrm{MJ\,m^{-3}}$ to around $30\,\mathrm{MJ\,m^{-3}}$. This increase in frictional dissipation with impact velocity is highly nonlinear and is responsible for the significant variation of peak temperatures observed in figure 7b.

Frictional dissipation also increases as the grain volume fraction η increases from 0.50 to 0.82 (figure 9c). However, this increase (from 10 to $40\,\mathrm{MJ\,m^{-3}}$ near the impact surface) is more gradual, in comparison with the increase associated with the impact velocity. Finally, the effect on frictional dissipation at $t = 3.6\,\mathrm{\mu s}$ of interface bonding strength in the range of $S_{max} = 8.75\text{--}35.0\,\mathrm{MPa}$ for $\eta = 0.82$ and $v_0 = 100\,\mathrm{m\,s^{-1}}$ is shown in figure 9d. At $T_{max} = 8.75\,\mathrm{MPa}$, frictional dissipation is higher and more stochastic, with local peak values reading up to $20\,\mathrm{MJ\,m^3}$, indicating that the formation of hot spots have significantly high temperatures.

Frictional dissipation typically occurs at later stages of loading and does not initiate until a t_d has elapsed (Barua *et al.* 2012). The delay time denotes the point at which the dominant heating mechanism changes from viscoelastic dissipation in the binder to frictional heating at fractured surfaces. The variation of delay time has been investigated previously for square samples subject to uniaxial loading (Barua & Zhou 2011b; Barua *et al.* 2012). Figure 10 shows the variation of delay time with grain volume fraction η in the range of 0.50–0.82 and impact velocity ranging from $v_0 = 100$ to $200\,\mathrm{m\,s^{-1}}$. For the same impact velocity, the delay strain decreases with grain volume fraction. At higher impact velocities, the delay time decreases by a similar amount for all grain volume fractions considered. During the delay time, the wavefront traverses a considerable length of the specimen. We find that the distance travelled by the wave in time t_d is quite insensitive to the grain volume fraction and is only dependent upon the boundary velocity. At $v_0 = 200$ and $100\,\mathrm{m\,s^{-1}}$, the corresponding distances are approximately $d_0 = 3.70$ and $5.44\,\mathrm{mm}$, respectively, for all volume fractions considered. This indicates that fracture and friction will not occur until the width of the stress wave exceeds d_0. It is noted that the initial ramp of loading can influence the overall delay time. Such loads with gradually increasing intensity initially can occur during impact because of surface roughness or impactor property gradation. However, regardless of whether a ramp is specified in loading, the trends outlined are applicable for the comparison of responses of materials with different microstructures under the same loading conditions.
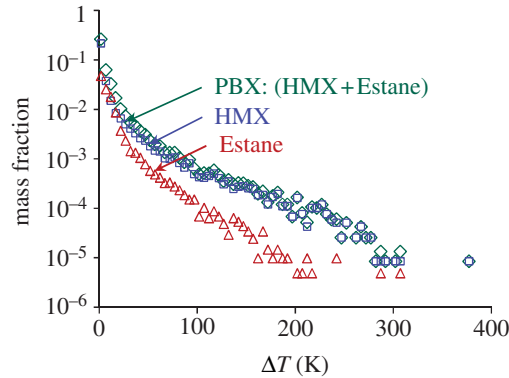
Figure 11. Temperature rises in the in grains and binder at $t = 3.6\,\mu s$ ($\eta = 0.82$, $v_0 = 200\,\mathrm{m\,s^{-1}}$). (Online version in colour.)

5. Temperature rises

The ignition sensitivity of the PBX is affected by several parameters, one of them being the mass fraction of the material having temperature rises above a certain value. The higher the mass fraction at elevated temperatures, the greater the probability for a sustained reaction. Histograms showing mass fraction as a function of temperature increase with temperature increments of $\Delta T = 5\,\mathrm{K}$ are used to provide an overall quantification of the heating in the material.

Figure 11 shows the temperature rises in the grains and matrix at $t = 3.6\,\mu s$ for a microstructure with $\eta = 0.82$ and a boundary velocity of $v_0 = 200\,\mathrm{m\,s^{-1}}$. The temperature rise profile shows a nonlinear trend with two distinct heating regimes. This can be explained on the basis of the bulk heating mechanisms. The lower end of the heating curve up to a temperature rise of approximately $50\,\mathrm{K}$ is dominated by viscoelastic heating in the binder. The viscous binder deforms easily and does not develop high stress until it is sufficiently deformed to allow higher stresses to result. The lower stresses in the binder lead to a relatively low amount of viscoelastic dissipation. The higher temperature regime is dominated by frictional dissipation. At the high end of the temperature spectrum, temperature rises of approximately 300–$400\,\mathrm{K}$ are seen. As mentioned earlier, high-temperature rises are primarily due to frictional dissipation in the grains. In the regime dominated by viscoelastic heating, the profile is relatively smooth. In contrast, the data in the high-temperature regime (more than $550\,\mathrm{K}$) show large oscillations, indicating a stochastic trend in the occurrence of spots associated with high temperatures. This is a result of the highly heterogeneous nature of the microstructure, and the fact that frictional dissipation is a surface phenomenon that occurs only at debonded or crack surfaces (figure 4d).

The evolution of temperature for a calculation with $\eta = 0.82$ and $v_0 = 200\,\mathrm{m\,s^{-1}}$ is shown in figure 12a. Initially at $t < t_\mathrm{d}$ (e.g. $1.4\,\mu s$), frictional dissipation has not initiated and the temperature rise is primarily due to viscoelastic dissipation in the binder. Consequently, the variation in temperature rise is small and the maximum temperature rise is approximately $50\,\mathrm{K}$. Higher temperature rises occur once frictional dissipation initiates. With time, the heating profile becomes increasingly nonlinear, with the initial viscoelastic regime followed by the friction-dominated heating regime.
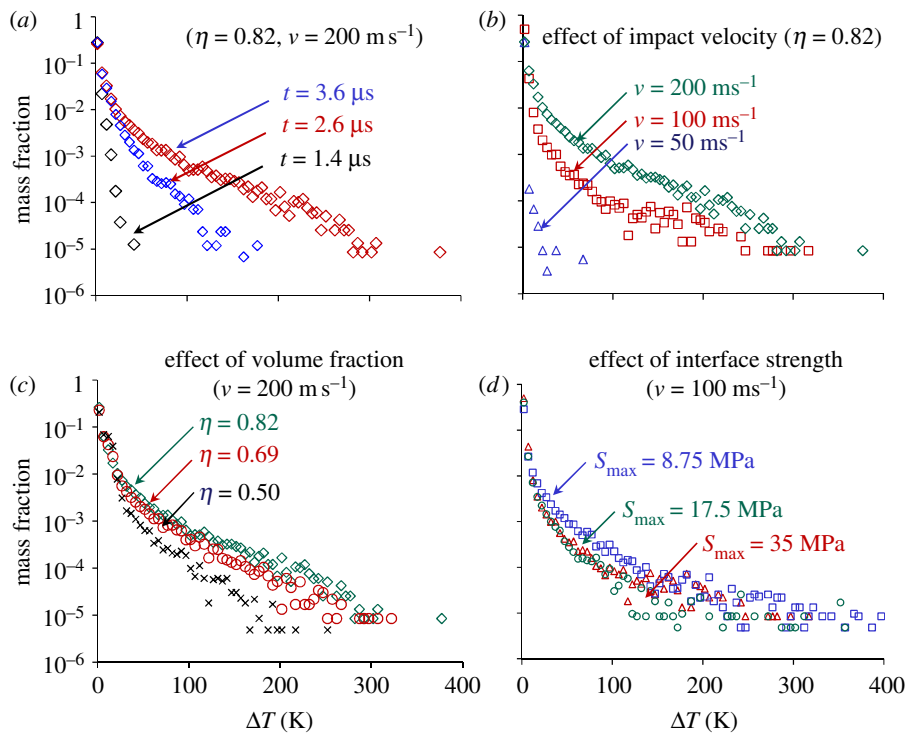
Figure 12. Temperature rises in the microstructure for (a) different times: $t = 1.4$–$3.6\,\mu$s ($\eta = 0.82$, $v_0 = 200\,\mathrm{m\,s^{-1}}$); (b) different impact velocities between $v_0 = 50$ and $200\,\mathrm{m\,s^{-1}}$ ($\eta = 0.82$); (c) different packing densities between 0.50 and 0.82 ($v_0 = 200\,\mathrm{m\,s^{-1}}$, $t = 3.6\,\mu$s); and (d) different interface strengths between $S_{\max} = 8.75$ and $35.0\,\mathrm{MPa}$ ($\eta = 0.82$, $v_0 = 100\,\mathrm{m\,s^{-1}}$, $t = 3.6\,\mu$s). (Online version in colour.)

As seen in §2, the dominant heating mechanisms can vary significantly with impact velocity. The temperature rise profiles at $t = 3.6\,\mu$s for $v_0 = 50$, 100 and $200\,\mathrm{m\,s^{-1}}$ and $\eta = 0.82$ are shown in figure 12b. At $50\,\mathrm{m\,s^{-1}}$, most of the heating is due to viscous dissipation in the binder and the maximum temperature rise is less than 60 K. As the impact velocity increases, the higher stresses increase viscoelastic and frictional dissipation. The increase in the frictional dissipation is quite significant and causes the mass fraction experiencing similar amounts of temperature rise to increase by an order of magnitude as the impact velocity increases from 100 to $200\,\mathrm{m\,s^{-1}}$. At an impact velocity of $100\,\mathrm{m\,s^{-1}}$, mass fractions having temperature rises greater than 100 K show more fluctuation and are more stochastic than in the case with $v_0 = 200\,\mathrm{m\,s^{-1}}$. This indicates that hot-spot temperatures are more uniform at higher impact velocities.

Figure 12c shows the temperature rises at $t = 3.6\,\mu$s for $\eta = 0.50$, 0.69 and 0.82 and $v_0 = 200\,\mathrm{m\,s^{-1}}$. The difference between the cases in the low-temperature regime ($\Delta T < 60\,$K) is not significant. Here, two counteracting mechanisms are at work. As the fraction of binder decreases, the average stresses in the material increases, resulting in higher viscoelastic dissipation. On the other hand, the mass of binder available for viscoelastic dissipation also decreases. These two trends balance out to cause the low-temperature portion of the heating curve to

remain approximately unchanged. However, the higher stresses at higher packing densities cause heat dissipation owing to a rise in frictional dissipation. As the grain volume fraction increases, the curve becomes more stochastic in the high-temperature regime, for reasons discussed previously.

Figure 12d shows the heating profiles at $t = 3.6\,\mu s$ for interface strength values of $S_{\max} = 8.75$, 17.5 and 35 MPa and $\eta = 0.82$ at $v_0 = 100\,m\,s^{-1}$. It has been shown earlier that the average stress in the compaction region is lower at lower interface strength, while behind the compaction region the average stress is similar for these cases. Overall, a decrease in interface bonding strength is associated with earlier debonding at the grain/matrix interface, more fractured surfaces for frictional dissipation, and higher temperature rises in the PBX.

6. Conclusions

This study focuses on the transient behaviour of HMX/Estane PBX under uniaxial strain conditions of boundary loading. Results show that the overall wave speed through the microstructures depends on both the grain volume fraction and interface bonding strength between the constituents and that the distance traversed by the stress wave before frictional dissipation initiates is independent of the grain volume fraction but increases with impact velocity. The analysis of stress profile showed that the average stress behind the compaction wavefront is highly sensitive to the volume fraction of the grains indicating that at higher grain volume fractions, the load is preferentially transmitted across neighbouring grains, resulting in much higher stresses. The average stress increases approximately linearly with the boundary velocity as a result of the rate dependence of the binder. On the other hand, it is insensitive to changes in interface bonding strength indicating closure effect of the compressive loading. For the time durations considered (5–6 μs) for which no wave reflection occurs, the fracture energy dissipated is highest near the impact face and decreases to zero at the stress wavefront. On the other hand, the highest temperature rises are approximately 2–3 mm from the loading surface. Scaling laws are developed for the maximum fracture energy dissipation rate and the highest temperature rise as functions of the impact velocity, grain volume fraction and grain–binder interfacial bonding strength. Analysis of the temperature rise shows that in the lower temperature regime dominated by viscoelastic heating, the profile is relatively smooth. By contrast, the data in the high-temperature regime show large oscillations, indicating a stochastic trend in the occurrence of spots associated with temperatures. The temperatures at the higher end of the spectrum are highly stochastic and may reach up to approximately 700–800 K for boundary velocities greater than $100\,m\,s^{-1}$. Such temperature rises suggest that impact at moderate velocities of the order of a few hundred microseconds may be sufficient for melting and reaction initiation.

References

Armstrong, R. W. & Elban, W. L. 1989 Temperature rise at a dislocation pile-up breakthrough. *Mater. Sci. Eng.* **122**, L1–L3. (doi:10.1016/0921-5093(89)90642-4)

Asay, B. 2010 *Non-shock initiation of explosives non-shock initiation of explosives.* Heidelberg, Germany: Springer.

Austin, R. A., McDowell, D. L. & Benson, D. J. 2006 Numerical simulation of shock wave propagation in spatially-resolved particle systems. *Model. Simul. Mater. Sci. Eng.* **14**, 537–561. (doi:10.1088/0965-0393/14/4/001)

Baer, M. R. 2002 Modeling heterogeneous energetic materials at the mesoscale. *Thermochim. Acta* **384**, 351–367. (doi:10.1016/S0040-6031(01)00794-8)

Barua, A. & Zhou, M. 2011*a* A Lagrangian framework for analyzing microstructural level response of polymer-bonded explosives. *Model. Simul. Mater. Sci. Eng.* **19**, 055001. (doi:10.1088/0965-0393/19/5/055001)

Barua, A. & Zhou, M. 2011*b* Heating in microstructures of HMX/Estane PBX during dynamic deformation. *Shock Compression Condensed Matter* **1426**, 1475–1478. (doi:10.1063/1.3686561)

Barua, A., Horie, Y. & Zhou, M. 2012 Energy localization in HMX-Estane polymer-bonded explosives during impact loading. *J. Appl. Phys.* **111**, 054902. (doi:10.1063/1.3688350)

Benson, D. J. & Conley, P. 1999 Eulerian finite-element simulations of experimentally acquired HMX microstructures. *Model. Simul. Mater. Sci. Eng.* **7**, 333–354. (doi:10.1088/0965-0393/7/3/304)

Benson, D. J., Tong, W. & Ravichandran, G. 1995 Particle-level modeling of dynamic consolidation of Ti-SiC powders. *Model. Simul. Mater. Sci. Eng.* **3**, 771–796. (doi:10.1088/0965-0393/3/6/003)

Dienes, J. K., Zuo, Q. H. & Kershner, J. D. 2006 Impact initiation of explosives and propellants via statistical crack mechanics. *J. Mech. Phys. Solids* **54**, 2235–2240. (doi:10.1016/j.jmps.2006.06.002)

Idar, D. J., Straight, J. W., Osborn, M. A., Skidmore, C. B., Phillips, D. S. & Buntain, G. A. 2000 PBX 9501 high explosive violent reaction: phase II baseline and aged experiments. See http://www.fas.org/sgp/othergov/doe/lanl/lib-www/la-pubs/00538217.pdf

Khasainov, B. A., Ermolaev, B. S., Presles, H. N. & Vidal, P. 1997 On the effect of grain size on shock sensitivity of heterogeneous high explosives. *Shock Waves* **7**, 89–105. (doi:10.1007/s001930050066)

Mas, E. M. & Clements, B. E. 1996 A viscoelastic model for PBX binders. See http://lib-www.lanl.gov/la-pubs/00818442.pdf

Menikoff, R. 2001 Compaction wave profiles: simulations of gas gun experiments'. Los Alamos, NM: Los Alamos National Laboratory.

Menikoff, R. 2004 Pore collapse and hot spots in HMX. In *Shock compression of condensed matter: 2003, pts 1 and 2, proceedings*, vol. 706 (eds M. D. Furnish *et al.*), pp. 393–396. Melville, NY: America Institute of Physics.

Panchadhara, R. & Gonthier, K. A. 2011 Mesoscale analysis of volumetric and surface dissipation in granular explosive induced by uniaxial deformation waves. *Shock Waves* **21**, 43–61. (doi:10.1007/s00193-010-0287-6)

Siviour, C. R., Gifford, M. J., Walley, S. M., Proud, W. G. & Field, J. E. 2004 Particle size effects on the mechanical properties of a polymer bonded explosive. *J. Mater. Sci.* **39**, 1255–1258. (doi:10.1023/B:JMSC.0000013883.45092.45)

Tarver, C. M., Chidester, S. K. & Nichols, A. L. 1996 Critical conditions for impact- and shock-induced hot spots in solid explosives. *J. Phys. Chem.* **100**, 5794–5799. (doi:10.1021/jp953123s)

Trott, W. M., Baer, M. R., Castaneda, J. N., Chhabildas, L. C. & Asay, J. R. 2007 Investigation of the mesoscopic scale response of low-density pressings of granular sugar under impact. *J. Appl. Phys.* **101**, 024917. (doi:10.1063/1.2427093)

Wu, Y.-Q. & Huang, F.-L. 2009 A micromechanical model for predicting combined damage of particles and interface debonding in PBX explosives. *Mech. Mater.* **41**, 27–47. (doi:10.1016/j.mechmat.2008.07.005)

Wu, Y. Q. & Huang, F. L. 2010 A thermal-mechanical constitutive model for B-HMX single crystal and cohesive interface under dynamic high pressure loading. *Sci. China Phys. Mech. Astron.* **53**, 218–226. (doi:10.1007/s11433-009-0264-1)

Zhai, J., Tomar, V. & Zhou, M. 2004 Micromechanical simulation of dynamic fracture using the cohesive finite element method. *J. Eng. Mater. Technol. Trans. ASME* **126**, 179–191. (doi:10.1115/1.1647127)